

Deposition penetration depth and sticking probability in plasma polymerization of cyclopropylamine

Miroslav Michlíček^a, Lucie Blahová^b, Eva Dvořáková^a, David Nečas^c, Lenka Zajíčková^{a,c,*}

^a Department of Physical Electronics, Faculty of Science, Masaryk University, Kotlářská 2, Brno 61137, Czech Republic

^b Plasma Technologies, CEITEC - Central European Institute of Technology, Masaryk University, Kamenice 5, Brno 62500, Czech Republic

^c CEITEC - Central European Institute of Technology, Brno University of Technology, Antonínská 548/1, Brno 60190, Czech Republic

ARTICLE INFO

Keywords:

Plasma polymerization
3D structured substrates
Bioactive functional coating
Penetration depth
Sticking probability

ABSTRACT

Understanding the role of substrate geometry is vital for a successful optimization of low-pressure plasma polymerization on non-planar substrates used in bioapplications, such as porous materials or well plates. We investigated the altered transport of film-forming species and properties of the coatings for a cyclopropylamine and argon discharge using a combined analysis of the plasma polymer deposition on flat Si pieces, culture wells, microtrenches, a macrocavity, porous hydroxyapatite scaffolds and electrospun polycaprolactone nanofibrous mats. The aspect ratio of the well structures impacted mainly the deposition rate, whereas the film chemistry was affected only moderately. A large deposition penetration depth into the porous media indicated a relatively low sticking probability of film-forming species. A detailed analysis of microtrench step coverage and macrocavity deposition disproved the model of film-forming species with a single overall sticking probability. At least two populations with two different sticking probabilities were required to fit the experimental data. A majority of the film-forming species (76%) has a large sticking probability of 0.20 ± 0.01 , while still a significant part (24%) has a relatively small sticking probability of 0.0015 ± 0.0002 . The presented methodology is widely applicable for understanding the details of plasma-surface interaction and successful applications of plasma polymerization onto complex substrates.

1. Introduction

Low-pressure plasma polymerization is inherently a complicated process involving a plethora of particle species and numerous effects governing their production, transport, deposition, and possibly removal [1]. Despite the complexity, plasma polymerization is from the technological standpoint a surprisingly robust process and has been studied for numerous applications ranging from optical coatings to bio-applications [2–5]. A simplified description of the plasma polymerization process which would correctly predict its main features and enable its successful up-scaling and application are therefore desirable but at the same time very difficult [6–8].

One of the approaches is the well-established macroscopic kinetics approach developed by Dirk Hegemann [9,7,10,11]. It links the complex plasma-chemical process in the non-isothermal plasma directly to the operating parameters of the reactor (e.g. power, gas flow or pressure) [10]. The macroscopic kinetics employs the concept of chemical quasi-equilibria described earlier by Rutscher and Wagner [12]. It states

that the specific energy consumed within the active plasma zone determines the excitation (active zone) and recombination (passive zone) processes leading to film growth. This enables the use of macroscopic kinetics. It is implicitly assumed that the deposition process is in the activation energy limited regime. Therefore, activation reactions can be described as having an overall energy barrier [11].

The macroscopic kinetics approach in principle enables the separation of gas phase effects and surface processes. In the quasi-Arrhenius regime, the gas phase chemistry remains mostly unchanged, just the reaction rate increases with the specific power W/F . Surface processes and most importantly ion bombardment depend on the power and other macroscopic variables in a more complicated manner through sheath potential, sheath collisional character, etc. [11]. Despite its apparent limitations, this approach has proven useful for getting insight and up-scaling of plasma polymerization processes [13].

On the other hand, when a plasma polymerization process is being tuned for a particular bioapplication, a mechanistic, “plasma as a black box” approach is often used, i. e., adjusting external plasma parameters

* Corresponding author.

E-mail address: lenkaz@physics.muni.cz (L. Zajíčková).

<https://doi.org/10.1016/j.apsusc.2020.147979>

Received 27 July 2020; Received in revised form 21 September 2020; Accepted 22 September 2020

Available online 27 October 2020

0169-4332/© 2020 The Author(s).

Published by Elsevier B.V. This is an open access article under the CC BY-NC-ND license

(<http://creativecommons.org/licenses/by-nc-nd/4.0/>).

to obtain a thin film to which the biological system displays the desired interactions [5,14,15]. This can be perfectly legitimate and sound, especially when we consider that the detailed mechanism of interaction of plasma polymer surface with the biological system is often also unknown. It might not be even clear what surface properties we actually want to achieve [16,14].

Coating of surfaces for bioapplications is further complicated by the need to process large batches. Plasma polymer film (PPF) properties are usually reported for one selected location in the reactor where a small piece of silicon is placed as the substrate. However, PPFs deposited across larger spatial distances generally cannot be considered uniform in thickness and more importantly homogeneous in chemistry [17,18]. Even if the plasma polymer deposition process is already optimized on a flat substrate, the complex geometry of surfaces to be coated can change the coating properties. In bioapplications the surfaces are often non-planar (e. g., tissue culture wells) or porous (e. g., scaffold and mats). The geometry can alter the gas flow pattern, plasma properties, and transport of species from plasma. It should be, therefore, also considered for a successful application of the plasma deposition process.

Recently, several papers emerged dealing with deposition into porous substrates, such as 3D printed scaffolds or nanofibrous mats [19–22]. The dominant mechanism for the transport of film-forming species into porous substrates is usually diffusion [21]. Unless the experiment is designed to produce a significant pressure drop across the porous substrate, the gas drift velocity is negligible. Especially at low pressure, the mean free path of gas species can be longer than or comparable with the pore size, meaning that the dominant transport mechanism is the Knudsen diffusion. The central quantity governing the penetration of the film deposition into the mat is then the sticking probability of the film-forming species. Although reliable coating of the internal surface of porous substrates is highly desirable [23,24], there is only a limited knowledge about sticking probabilities, particularly for more complicated chemistry of species and substrates.

In this paper, we investigate some fundamental aspects of plasma polymerization onto 3D structured substrates commonly used in bioapplications, such as various culture wells and porous materials, employing a combination of “black-box” and macroscopic kinetics approaches. Using the example of discharge in non-toxic cyclopropylamine (CPA) [25,26] in argon, we show the effects of well geometry on the film deposition rate and chemistry. Furthermore, deposition penetration into porous substrates is investigated. The discussion is supported by experiments to estimate the effective sticking coefficient for the film-forming species in the CPA/Ar discharge and by a critical evaluation of the approximation of a single effective sticking coefficient for the chemistry of a film deposited into a macrocavity.

2. Methods

2.1. Plasma polymerization of CPA

The cyclopropylamine PPFs were deposited in a capacitively coupled radio-frequency (RF) discharges ignited in a UHV reactor between parallel plate electrodes, 210 mm in diameter. The distance between the electrodes was 55 mm. The bottom electrode holding the substrates was driven by an RF generator working at the frequency of 13.56 MHz and therefore negatively DC self-biased. The flow rate of CPA vapors (98% purity, Sigma Aldrich) was set to 1.0 sccm by a needle valve. The argon flow was chosen at 10 sccm, so that the residence time in the reactor was similar to our previous experiments in a similar discharge [5]. The pressure in the chamber was 50 Pa, and the leak rate was below 0.01 sccm. Depositions labeled CW were performed with continuous power, whereas PW denotes square pulsed wave with repetition frequency of 500 Hz and 33% duty cycle. The default RF power was pulsed wave 40 W (40W-PW), referred to as the standard conditions. The self-bias voltage for a typical continuous wave discharge with the power of 40 W was about 40 V. The deposition time for different conditions was

adjusted to deposit approximately 250 nm thick films on a flat surface.

2.2. Substrates

A few different substrates were used for the CPA PPF deposition as described below. Pieces of monocrystalline silicon (N-type, orientation 100, 525 μm , double-side polished) were placed directly on the driven electrodes or into well structures used in biological experiments. These included polystyrene Petri dishes (PD), CellCrown™ inserts (CC) and 96-well plates (WP). Their diameters D , heights H and aspect ratios $AR = H/D$ are summarized in Fig. 1a.

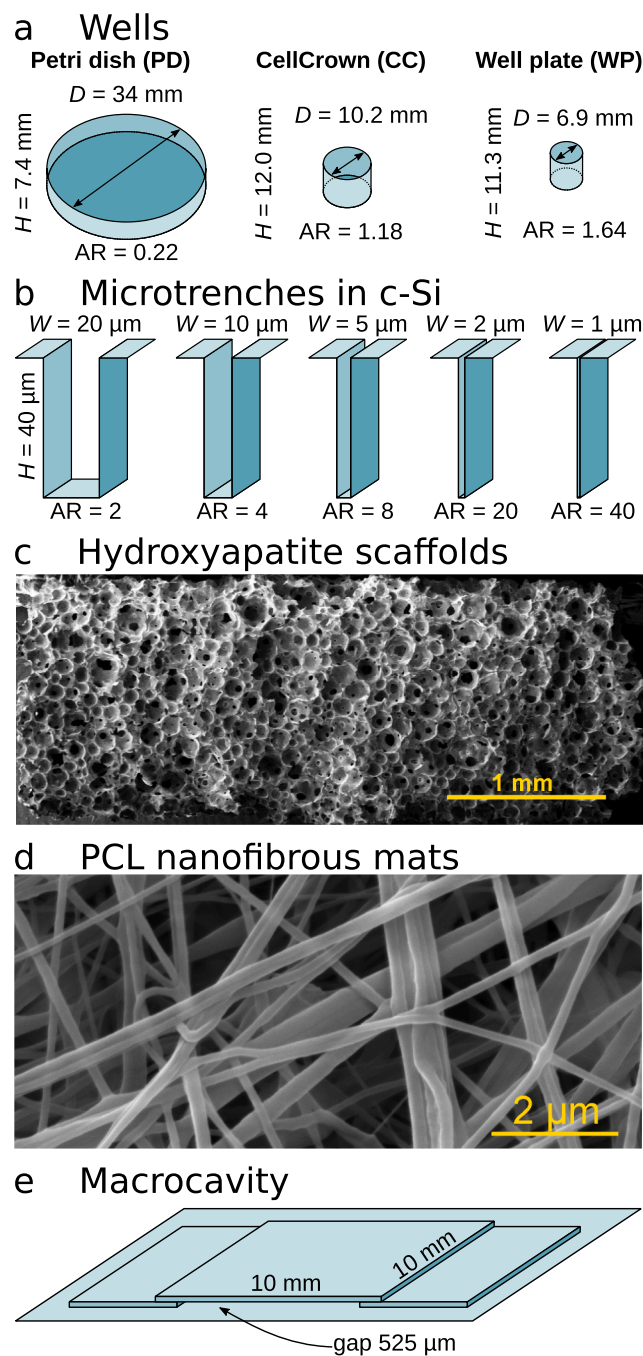


Fig. 1. Summary of used substrates. Wells (a) and Si microtrenches (b) are shown with true aspect ratios. Hydroxyapatite scaffold (c) and PCL mat (d) are shown as SEM micrographs. Macro cavity (e) prepared from silicon pieces forming a bridge is drawn schematically.

2.2.1. Microtrenches in c-Si

Microtrench structures were prepared by standard photolithography procedures for high aspect ratio etching. The height of the trenches was approximately 40 μm ; the widths were about 20, 10, 5, 2, and 1 μm , as schematically summarized in Fig. 1b. Due to the manufacturing imperfections, the dimensions and aspect ratios of prepared microtrenches were slightly different and were measured by SEM for each particular microtrench.

2.2.2. Hydroxyapatite scaffolds

Porous hydroxyapatite (HA) scaffolds were supplied by Aimedica MMT, Tokyo under trade name Neobone™ (molecular formula $\text{Ca}_{10}(\text{PO}_4)_6(\text{OH})_2$, purity of 99.9%). The scaffolds were used as received. Note that XPS revealed carbon contamination [C] \approx 40 at.% on the scaffold surface. The HA overall porosity was \approx 72–78% with an average spherical pore diameter of \approx 150 μm and pore interconnections of \approx 40 μm . Disc shape samples with a diameter of 5 mm and a thickness of 2 mm were used in our experiments. SEM micrograph of the scaffold cross-section is shown in Fig. 1c, for detailed view see also Fig. S1 in the Supplementary material (SM).

2.2.3. Polycaprolactone (PCL) nanofibers

Nanofibrous mats were prepared by electrospinning of polycaprolactone (PCL) as described in our previous publication [27]. The average diameter of individual nanofibers was $(270 \pm 60)\text{nm}$ as measured by SEM, with relatively uniform distribution. The average pore diameter was estimated also by SEM to \approx 1 μm . SEM micrograph of a representative surface is given in Fig. 1d. Pieces of about $1 \times 8\text{cm}^2$ were cut from prepared sheets and masked by tape from sides and from the bottom to prevent the diffusion of film-forming species from the respective directions. Similarly as in [27], we used edges of the PCL mats which naturally exhibit thickness gradient and after peeling it from the support we used the backside of PCL mats for analysis. The mats were used as prepared without further cleaning. The mat thickness was afterward measured by micrometer screw gauge with a ratchet thimble.

2.2.4. Macrocavity

A macrocavity in the shape of a slit was prepared using three silicon pieces forming a bridge on a larger silicon piece, as depicted in Fig. 1e. The macrocavity height was defined by the Si piece thickness of 525 μm , the lateral dimensions were chosen as $10 \times 10\text{mm}^2$.

2.3. Characterization methods

2.3.1. Spectroscopic ellipsometry

The PPF deposited on silicon pieces were characterized by ellipsometry using a rotating analyzer ellipsometer VASE (Woollam) operating in the spectral region of 1.0–6.5 eV at the incidence angle of 65° . Additionally, spatially resolved line scan measurements were acquired by a UVISSEL phase modulated ellipsometer (Horiba Jobin). The spectral dependencies of ellipsometric parameters were measured for the incidence angle of 65° within the spectral range 1.5–5.5 eV. The data were fitted using a PJDOS dispersion model for amorphous materials [28] and a structural model accounting for the large thickness non-uniformity [29]. It allowed calculating the local film thickness and its gradient as well as dispersion parameters determining the spectral dependencies of the optical constants of the PPF.

2.3.2. SEM

The samples were imaged using the field-emission scanning electron microscope (FE-SEM) LYRA3 XM, manufactured by Tescan. The electrons were accelerated by a 5–10 kV high voltage and the working distance was fixed to 9 mm. Images of at least 1024×1024 pixels were acquired within 2 min.

2.3.3. FTIR

The transmittance in the spectral range from 400–4000 cm^{-1} was measured using an FTIR Bruker Vertex 80v spectrophotometer with a parallel beam transmittance accessory. The data were collected at the pressure of 250 Pa with the resolution of 4cm^{-1} and 500 scans. The transmittance of the films on a Si substrate was divided by the transmittance of the bare Si substrate in order to calculate a relative transmittance. After subtracting the background, Beer–Lambert's law was applied to calculate the absorption coefficient.

2.3.4. XPS

The X-ray photoelectron spectra (XPS) for a surface chemical characterization of CPA PPF were acquired with the Axis Supra spectrometer (Kratos Analytical, England). To avoid differential charging of samples, spectra were acquired with a charge neutralization in overcompensated mode. The spectra were subsequently normalized by shifting the aliphatic carbon component to 285.0 eV. The quantitative composition was determined from detailed spectra taken at the pass energy of 20 eV. Fitting of the high-resolution spectra was done based on the model adopted from the paper of Truica-Marasescu and Wertheimer [30] with an additional peak for highly oxidized carbon COOR at 288.9 eV. The standard large area measurements were acquired with the slot aperture (dimensions $700 \times 300\text{ }\mu\text{m}$). Finer spatial details were resolved using a smaller cylindrical aperture of 110 μm in diameter.

2.4. Simulation details

We performed a simple Monte Carlo particle-tracing simulation of the deposition to evaluate thin film step coverage in microtrenches. The model assumed that surface reactions are limited to desorption and adhesion, with probability expressed by the reactive sticking coefficient. The dimensionality of the problem was reduced by assuming periodic grating-like structure with infinitely long trenches. The particles were traced in a square simulation box (Fig. S2 in the SM). The sidewalls of the simulation box were reflective, representing the second half of the microtrench, which was not explicitly present in the simulation, and the periodic condition. The particles were introduced into the box one by one with a random position at the upper side and random direction of motion. In each simulation step, a finite movement length was drawn from an exponential distribution given by the mean free path, and the particle was moved accordingly, unless it hit the trench surface or simulation domain boundary. Particles passing through the top boundary were considered lost and discarded. Particles hitting the reflective boundary were reflected. The trench surface was sticky with the sticking probability η . If a particle hitting the trench was evaluated as sticking, film growth was noted at its position and a new particle was generated. Otherwise, the desorbing particle continued moving in a new random direction that was drawn according to the cosine law. The effect of the film growth on the trench geometry was not considered.

The simulation box had to extend sufficiently above the top surface (compared to the mean free path) in order to account correctly for particles returning to the surface due to gas phase collisions. Based on our analysis, the vertical dimension of ten mean free paths was sufficient to obtain converged results, i. e., the step height coverage no longer changed with a further increase of the box size. Therefore, we chose this simulation domain size to reduce computational time.

3. Results

3.1. Thickness uniformity and chemical homogeneity

The thickness uniformity and chemical homogeneity of the deposition were studied on pieces of silicon placed along the radius of the driven electrode. Fig. 2 shows results for the standard conditions – pulsed discharge with the nominal power of 40 W (40W-PW). The sample analysis by ellipsometry revealed poor deposition thickness

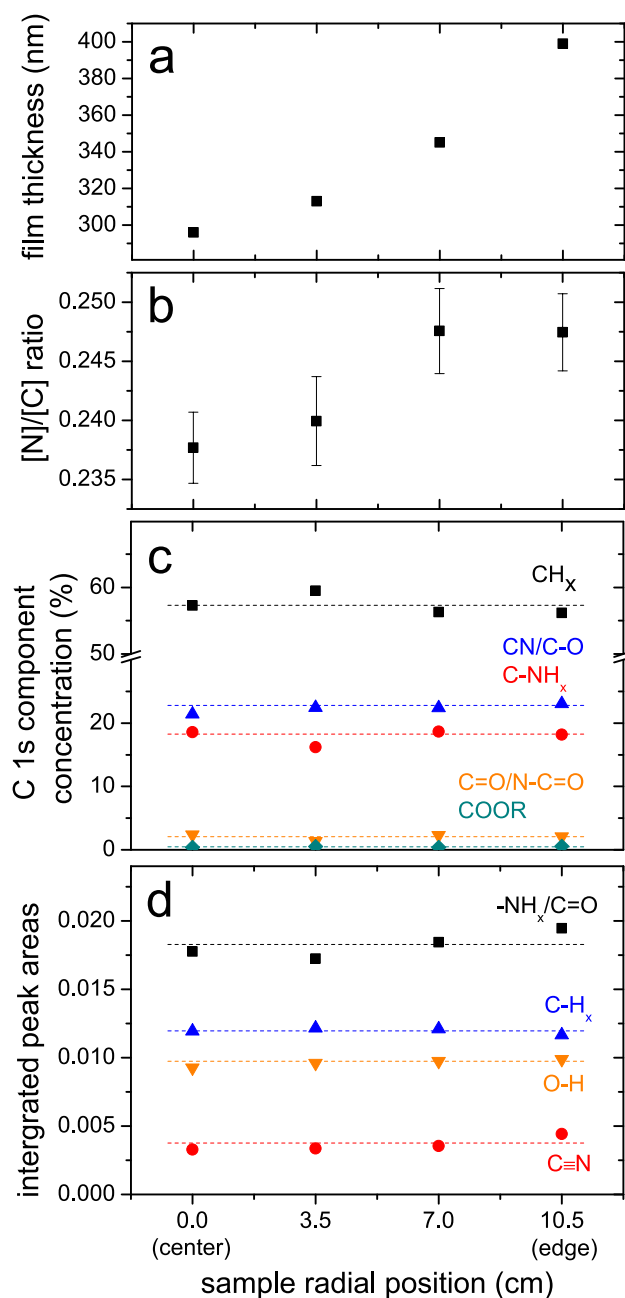


Fig. 2. Comparison PPF thickness (a), [N]/[C] measured by XPS (b), fitted components of high-resolution C 1s XPS spectra (c), and FTIR peak intensities (d) of samples placed across radius of the driven electrode in the R4 reactor. Discharge power 40W, pulsed. Lines representing mean values were added as guide to the eye in plots c and d.

uniformity, with deposition rate increasing by about 35% from the electrode center towards the edge (Fig. 2a), where the plasma is visibly more intense due to the adjacent grounded electrode collar. However, surface chemical analysis by XPS showed only a slight increase in the [N]/[C] ratio (Fig. 2b), which could be considered as a simple “rule of thumb” for the incorporation of nitrogen functionalities. At the same time, fitting of high-resolution C 1s peaks showed that the relative concentrations of functional groups remained the same within the estimated uncertainties (Fig. 2c). Similarly, the FTIR results (Fig. 2d) showed that concentrations of selected functional groups remained constant. Overall, we observed relatively small changes in the sample chemistry despite large variations in the deposition rate. The relatively more uniform central area of the electrode was selected for further

experiments comparing the deposition rates inside different non-planar samples.

3.2. Deposition into well structures

In Fig. 3a we compare the deposition rates on pieces of Si placed in a Petri dish (PD), CellCrown™ (CC) and well plate (WP) relative to the thickness deposited on Si placed directly on the driven electrode. At a higher average RF power some wells collected dust from the plasma, which is denoted by a bullet sign. Free particles were blown off the surface before the analysis but some particles were embedded in the thin film.

The deposition rate in the wells was always lower than directly on the electrode. Even for a wide and shallow structure such as Petri dish (aspect ratio $AR = 0.22$), the deposition rate was reduced to less than 75%. For higher aspect ratio wells the deposition rate continued to decrease – only moderately to 40–60% for the CC well ($AR = 1.18$) and very noticeably to 10–15% for WP wells. Note that CC and WP wells have similar heights and the difference in AR is given by the smaller diameter of the WP wells.

Fig. 3b shows how the change of the well geometry translates into the PPF composition expressed by the [N]/[C] ratio. For the pulsed input power of 20W (20W-PW), the discharge deposits the overall highest nitrogen content which is the same on all samples within the margin of error. A higher average RF power (40W-PW) resulted in a lower [N]/[C], which remained the same for samples in wells, with the exception of the CC well. The highest average RF power obtained by continuous power of 40W (40W-CW) led to the lowest overall [N]/[C], which was decreasing further with increasing AR of the wells.

3.3. Penetration into porous HA scaffolds

Fig. 4 shows elemental concentration profiles in the HA scaffolds after the deposition with standard conditions (40W-PW) measured by XPS along the sample rotational axis (see Fig. S3 in the SM for the measurement scheme). Among the detected elements, only nitrogen provides direct evidence of PPF presence, as both carbon and oxygen are found in pristine HA scaffolds. The scaffold simply placed on the

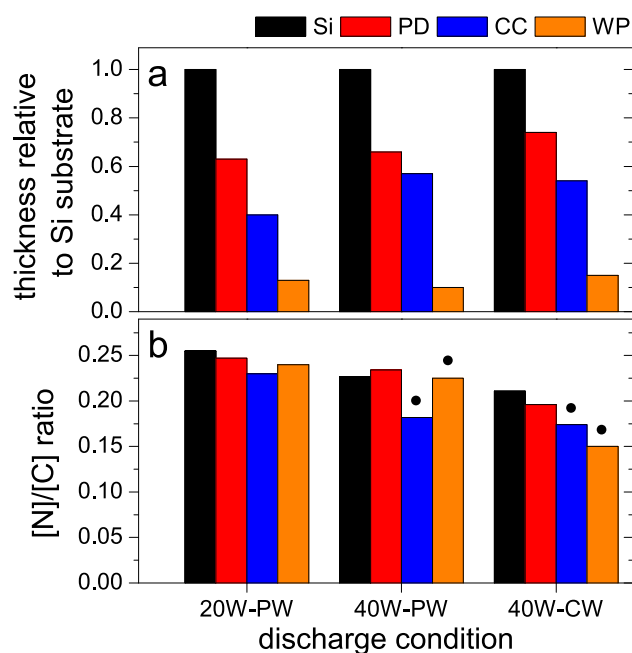


Fig. 3. Deposition rate in well structures relative to the thickness deposited on silicon placed directly on the electrode (a) and [N]/[C] ratio measured for the same samples (b). Bullet sign denotes visible powder present on the surface.

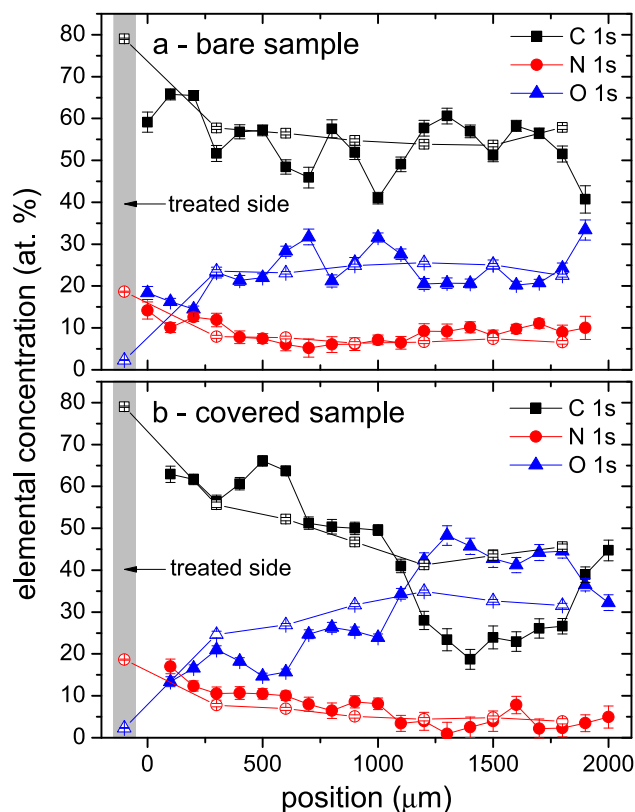


Fig. 4. Concentration of elements measured by XPS along the axis of cut bare (a) and covered (b) HA scaffolds. Empty symbols denote large area scans, while full symbols stand for 110 μm scans. Calcium and potassium are omitted from the graphs for clarity.

electrode (Fig. 4a) shows a decrease of nitrogen concentration in the first few hundred micrometers and remains stable at ≈ 7 at.% at higher depths, confirming the deposition penetration into the whole volume of the HA scaffold.

To simplify the geometry we performed a similar experiment where the sidewalls and the bottom of the HA scaffold were masked by Kapton tape, preventing diffusion of film-forming species from these surfaces. In this case, the nitrogen concentration profile (Fig. 4b) gradually decreases close to the limit of detection in about half of the sample thickness.

3.4. Penetration depth into PCL nanofibrous mats

Fig. 5 shows nitrogen concentration measured on the backside of nanofibrous mats after deposition and peeling them off the support. Two sets of mats were used to cover a larger range of thicknesses, $< 35 \mu\text{m}$ and $> 35 \mu\text{m}$, as indicated by the separating line. The nitrogen concentrations in the top surfaces range from 12 at.% to 18 at.%, depending on the discharge power and mode. For each discharge condition, the original nitrogen concentration steadily decreases with the mat thickness. The decrease compared to the top surfaces is just a few atomic percent for the thinnest mats ($\approx 20 \mu\text{m}$). For the thickest mats ($\approx 90 \mu\text{m}$) nitrogen is still detectable at about 0.5 at.%. The data in Fig. 5 for thinner and thicker mats form two distinct groups for each condition, differing by the slopes of the dependencies. Although both mat types were prepared with the same recipe, their structure and porosity differ due to a slightly different process condition (humidity and temperature) or different drying due to different mat thicknesses.

The effective deposition penetration depth was estimated by fitting the nitrogen concentration for each plasma condition with a simple exponential function. The fit predicted a relatively large characteristic

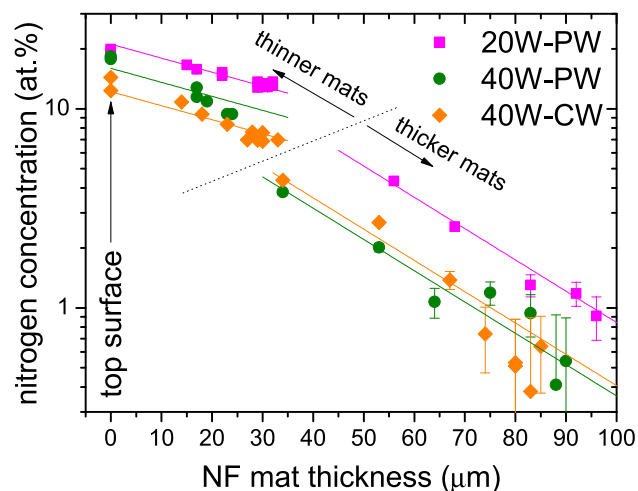


Fig. 5. Nitrogen concentration measured by XPS on the backside of nanofibrous mats plotted versus the mat thickness. Straight lines represent fit with an exponential decay model assuming the same slope for the thinner and thicker mats separately.

decay length, i. e., the penetration depth, of about 30–70 μm . This value comes mostly from data for high nitrogen concentrations because they have small estimated uncertainties. However, XPS uncertainties account only for random Poisson noise in the XPS data and do not reflect other error types. The estimated uncertainties of high nitrogen concentration are thus too small and consequently their fitting weights too large. For more realistic estimates the relative fitting weights would not differ so much between low and high concentrations. In the limit of comparably large errors, equivalent to unweighted fitting, the fit leads to mutually more consistent penetration depths of 23–30 μm .

Alternatively, we can consider the thinner and thicker mats separately. According to Fig. 5 the same slope can be then assumed for either set for all discharge conditions. This model highlights the already noted difference between the two sets of mats, yielding the penetration depth $\approx 60 \mu\text{m}$ for thinner mats and $\approx 30 \mu\text{m}$ for the thicker mats.

3.5. Estimation of the effective sticking coefficient

The effective sticking coefficient was estimated on the basis of step coverage of microtrenches etched in crystalline silicon with aspect ratio varying from about 2 to 40. If the sticking probability is high, the film-forming species are deposited on the walls before reaching the bottom. In contrast, the same thickness is deposited everywhere for the limit of low sticking probability. The thickness of the PPF deposited in a microtrench was measured by SEM of the microtrench cross-section prepared by its breakage (Fig. S4 in the SM). The results are plotted in Fig. 6a. The step coverage, defined as the ratio of the film thicknesses on the trench bottom and outside, is decreasing from about 0.5 for the aspect ratio $H/W \approx 2$ to less than 0.1 for the highest aspect ratio $H/W \approx 40$. All discharge conditions show a similar step coverage (within estimated uncertainties). Therefore, also the effective sticking probabilities are considered the same. The thickness uncertainties are relatively large for PPFs deposited on the bottoms of narrow trenches because the films were very thin to ensure that all film thicknesses are much smaller than the trench dimensions.

The sticking coefficient was estimated by the formula for step coverage SC in CVD deposition driven by Knudsen diffusion [31]:

$$SC = \frac{1}{\cosh\phi + \sqrt{3\eta/8} \sinh\phi}, \quad \phi = \frac{H}{W} \sqrt{\frac{3\eta}{2}}, \quad (1)$$

where H and W are the trench height and width, and η is the sticking probability. Note that formula (1) differs from the original published

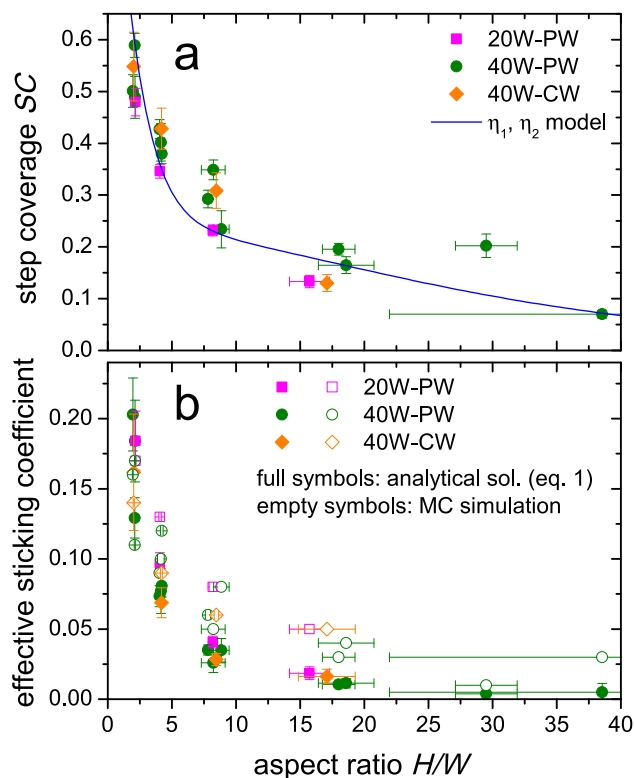


Fig. 6. Measurement of the step coverage SC (a) and estimate of the effective sticking probability η (b) for CPA/Ar deposition for selected conditions. Blue line in graph a correspond to the best fit with a model described in Section 4.4. Full symbols in the graph b denote η evaluated by formula 1, while empty symbols represent η estimated on basis of the particle simulation.

version because the paper [31] contained a misprint (the corresponding graph was correct). Since the derivation of formula (1) is based on the diffusion equation, it implicitly assumes that the trench depth is much larger than the mean free path of the depositing species. This condition is not satisfied in our case. Therefore, the step coverage was calculated also by the Monte Carlo simulation described in Section 2.4 (see Fig. S5 in the SM for the simulation results). The effective sticking probabilities deduced from both methods are compared in Fig. 6b. The simulation estimates a higher sticking probability than the analytical solution for the same parameters. Nevertheless, considering that we want to obtain merely an estimate, the agreement is reasonable. Regardless of the method, the effective sticking probability shows a decreasing dependence with H/W , from approximately 0.2 for the lowest H/W to about 0.01 for the highest H/W . We further discuss this dependence in Section 4.4.

3.6. Macro cavity deposition

The macro cavity experiment provided a sample for the analysis of a thin film deposited by Knudsen diffusion in the standard conditions (40W-PW). To minimize the laminar flow, the macro cavity openings were oriented perpendicular to the outside gas flow in the electrode radial direction. Although the macro cavity height 525 μm was larger than the gas mean free path of about 100 μm , each film-forming species is expected to interact with the macro cavity inner surface numerous times similarly as in the microtrenches.

Fig. 7 shows film characteristics measured along the axis of the macro cavity indicated in Fig. 7a with a red dashed line. The thickness measured by mapping ellipsometry is plotted in Fig. 7b, the elemental composition in Fig. 7c and fitting of the C 1s peak in Fig. 7d. Since we do not observe any asymmetry of film thickness, the macroscopic flow

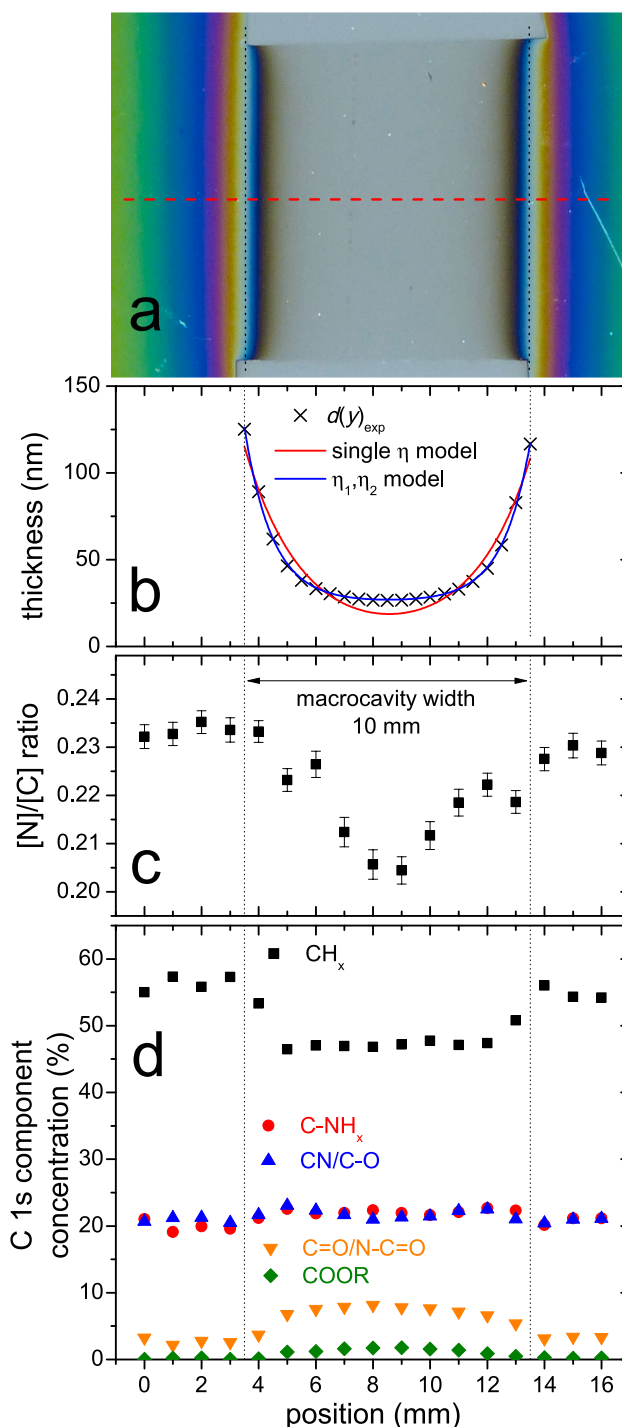


Fig. 7. Macro cavity deposition experiment. Figure a shows photo of the coated and disassembled macro cavity, red dashed line denotes axis along which the thickness profile (b) and XPS elemental composition (c) and high resolution XPS C 1s component (d) were analyzed. Blue line in graph b correspond to the best fit with a model described in Section 4.4. (For interpretation of the references to colour in this figure legend, the reader is referred to the web version of this article.)

through the macro cavity was negligible. At the macro cavity edges the thickness steeply decreases already in the first few millimeters and remains almost constant, $\approx 30\text{nm}$, in the macro cavity center. Similarly as for the microtrenches, the thickness of PPF deposited in the macro cavity can be fitted to an analytical solution of the diffusion equation. If we chose the macro cavity center as origin of coordinate y , we obtain a

simple formula for the relative thickness:

$$\frac{h(y)}{h_0} = \frac{\cosh(\alpha y)}{\cosh(\alpha L/2)}, \quad \alpha = \frac{1}{H} \sqrt{\frac{3\eta}{2}}, \quad (2)$$

where $h(y)$ is the film thickness, L and H are the macrocavity length and height (here 10 and 0.525 mm, respectively), $h_0 = h(\pm L/2)$ is the film thickness at the macrocavity boundary, and η is the effective sticking probability. The best fit of the data, drawn as the smooth red line in Fig. 7b, predicts the effective sticking probability $\eta = 0.045 \pm 0.005$. However, the model fits the data poorly and must be refined, as we will do in Section 4.4.

Interestingly, the elemental composition in the macrocavity measured by XPS shows only a small variation of [N]/[C], about 0.02. The film composition at the macrocavity boundary did not exhibit any sharp change, even though only the outer side is subject to ion bombardment. Fitting the C 1s peak shows again rather small differences, but apparently contradicting the elemental analysis. Although the nitrogen and oxygen concentrations decrease inside the macrocavity, the concentration of carbon bonded in functional groups, particularly C=O or N-C=O, slightly increases while aliphatic carbon decreases. Because fitting the nitrogen and oxygen environments does not show any major differences we propose that it is an effect caused by a surface vertical differential charging during XPS analysis [32]. We hypothesize that the charge neutralization fails for very thin films. A part of the analyzed material, e. g., close to the underlying grounded silicon, then has the ground potential instead of a slightly negative. This is supported by the observation that the C=O/N-C=O component in the C 1s peak is positioned at about 284.5 eV before the charge compensation and, therefore, is enhanced by signal of grounded aliphatic carbon.

4. Discussion

4.1. Deposition regimes

In a typical low-pressure plasma polymerization, the deposition is taking place practically everywhere in the reactor and, in general, the deposited layer properties can differ from place to place [17,18]. However, for some processes the chemistry of deposited coating remains practically the same everywhere as long as the ion bombardment on the coated surfaces remains the same [33]. This is the case of our deposition process from the mixture of CPA an Ar. In Fig. 2 we report the deposition rate increase by 35% from the center to the electrode edge and assume it is caused by the more intense local activation due to more intense plasma near the edge of the electrode. However, the elemental concentrations show only a slight change (Fig. 2b) and concentration of chemical groups remain constant within the errors (Fig. 2c-d).

Our observation can be explained by two mechanisms, the well-mixed reactor model or the macroscopic kinetics model assuming the energy-deficient deposition regime with a single overall plasma-chemical pathway [10,11]. Nevertheless, we can argue that the film-forming species are not well-mixed in our system. At low pressure, the gas flow is typically laminar and, therefore, the dominant mixing mechanism is diffusion. The diffusion coefficient can be estimated from the kinetic radii of the molecule and its diffusion partner. For our system (CPA in argon, 50 Pa) we estimated $D(\text{CPA}) \approx 200 \text{ cm}^2/\text{s}$. The diffusion length can then be estimated from the species lifetime. As the upper limit, we can consider the residence time of the gas in the reactor, which is $\approx 1 \text{ s}$. From this, we get the diffusion length of CPA in argon comparable to the chamber dimensions ($\approx 20 \text{ cm}$). Therefore, CPA itself is well mixed and it can contribute to the film growth since it can polymerize via the radical mechanism. However, activated film-forming species such as radicals have to be assumed to have considerably shorter lifetimes. Therefore, for film-forming species the diffusion should be limited to much shorter distances and the hypothesis of well-mixed reactor seems unlikely. This is supported by the PPF thickness nonuniformity,

which can only arise if the diffusion length is shorter.

Thus, we can conclude that the deposition is in the quasi-Arrhenius regime, i. e., the overall plasma polymerization pathway does not change when more energy is locally supplied to the plasma. A higher local power density increases the electron density which in turn increases monomer activation. Increased activation then results in a higher deposition rate. Because the thin film chemistry does not change, it can be described by an Arrhenius plot with a single activation energy. This is not generally true for all plasma polymerization mixtures. Some monomers were shown to have a more complicated overall chemical pathway that cannot be described by a single overall activation energy [34,35].

4.2. Deposition into well structures

The boom of applications of functional plasma polymers in biological field requires a consideration of experimental aspects connected with the deposition into well structures such as Petri dishes or cell culture wells. The deposition inside such cavities generally differs from the deposition on a flat surface due to the altered geometry. The overall gas flow pattern above the sample should not change significantly for the samples that are small relative to the inter-electrode gap. However, the well walls limit direct gas flow over the well bottom surface, moving the effective boundary for the diffusion of film-forming species further from it. Moreover, unless the width W of the cavity is much larger than the Debye length ($\approx 0.3 \text{ mm}$), plasma cannot extend into the cavity (CC and WP wells), and the plasma sheath is further from the bottom surface. Therefore, the well geometry changes the ion bombardment, geometry and boundary conditions for the diffusion of film-forming species.

The relative reduction of PPF thickness in wells (Fig. 3) is mostly affected the well geometry. The dependence on the discharge condition is not clear which prevents us to draw a conclusion on the dominant effect governing the deposition rate reduction.

From the application point of view, the chemistry of PPFs deposited in the wells is much more important than thickness variation. We have shown that the PPF [N]/[C] ratio in the three types of wells is less or equal to the [N]/[C] for silicon piece (Fig. 3) but the [N]/[C] changes do not result at the first glance into a clear conclusion about the influence of well structure on the nitrogen incorporation. Two main processes can be responsible for the changes in the PPF [N]/[C]. First, the nitrogen-containing film-forming species could have on average a higher sticking probability, making them more likely to be deposited before reaching the well bottom. Alternatively, the ion bombardment could have an enhancing effect on the incorporation of nitrogen by the surface activation. However, since the plasma does not penetrate inside the well, the effective plasma sheath thickness is increased and the ion bombardment is reduced by collisions. Based on the macrocavity experiment (Fig. 7) we can discard the effect of ion bombardment on the chemistry, as there was no sharp change in the chemistry at the macrocavity edge. The [N]/[C] profile in the macrocavity supports a slightly higher sticking probability of the nitrogen-containing film-forming species for the standard conditions (40W-PW) but yet it cannot explain the significantly lower nitrogen concentration sometimes observed in the higher aspect ratio wells. This discrepancy might be caused by powder which is preferentially collected during the deposition in a well depending on the aspect ratio [36]. The powder created in the gas phase can be expected to have a different chemical composition than PPF grown on the electrode, namely because of high powder temperature and therefore faster decomposition of nitrogen-containing groups [37].

4.3. Deposition penetration depth into porous substrates

There is an interesting difference between the penetration of plasma deposition into porous materials such as porous HA scaffolds and PCL nanofibrous mats. Both are porous materials used for tissue engineering that might require a surface modification thus, penetration of the plasma

polymerization into these substrates is highly desirable. While the HA scaffolds can directly benefit from enhanced cell adhesion, pores in PCL mats are too small for cells. However, the inner mat surface can be used for drug loading, synergizing with enhanced surface cell colonization.

The HA scaffold has a highly interconnected structure resembling a foam created by relatively large spherical cavities, $\approx 150 \mu\text{m}$ diameter, each with several interconnects of about $40 \mu\text{m}$ (Fig. 1c, for detailed view see also Fig. S1 in the SM). The mean free path at the pressure of 50Pa is larger than $100 \mu\text{m}$, i. e., comparable with the scaffold pore size, suggesting that transport inside the scaffold is driven by Knudsen diffusion. Therefore, any film-forming particle which was able to penetrate deep into the scaffold undertook numerous interactions with the surface, and their sticking coefficient has to be small.

Despite the obvious scale difference, gas transport in the two porous materials can be comparable. The typical cavity or pore size in PCL mats is much smaller than in HA scaffolds (by a factor of at least 40). On the other hand, the mats are much thinner (typically by a factor of 20). Although details of Knudsen transport in porous media are very complicated, the main scaling parameter for the transmission probability through the pores is the ratio of the pore diameter to the length [38]. In the first approximation the dimension factors almost cancel out and we can expect a similar diffusion profile.

In our recent paper, the deposition penetration into PCL mats was studied for atmospheric pressure DBD discharge in a mixture of maleic anhydride and acetylene [27]. We observed a similar deposition penetration depth into the PCL mats as in this work and hypothesized that the deposition could be caused by local activation of the gas mixture by streamers passing through the pores. However, in the low pressure discharges studied here, the effect of local activation of monomer in the mat structure can be ruled out. The Debye length and plasma sheath are much larger and plasma cannot penetrate into the pores. Therefore, the penetration depth in the range of tens of micrometers leads to conclusions that some nitrogen-containing film-forming species had undergone numerous collisions with the surface and that the sticking coefficient is relatively low. This was confirmed also by the microtrench step coverage experiments (Fig. 6).

The decrease in nitrogen concentration can be explained by two plausible mechanisms, change of the PPF chemistry and reduction of thickness below the XPS information depth. However, the change of the PPF chemistry can be disproved by the following discussion. The sticking probability of various film-forming species can be generally different. If the nitrogen-containing film-forming species had on average a higher sticking probability, it would lead to a faster depletion of these species, creating a gradient in the elemental composition. However, the macrocavity experiment which is analogous to this situation showed only a mild gradient in the PPF composition.

The correct explanation is, therefore, that the drop of nitrogen concentration in the scaffolds is caused predominantly by a decrease of the PPF thickness below the XPS information depth of about 5nm . Since the underlying substrate is also detected, the effective nitrogen concentration is reduced. In the case of PCL mats, we can further support it by the observation of the C 1s and O 1s spectral shapes characteristic for the underlying PCL in the samples with the nitrogen concentration below about 5at.% (SM Fig. S6). For the HA scaffold, such argument is not possible because cutting the substrate uncovers the pristine HA surface. Nevertheless, we assume that also in this case the detected nitrogen originates from a sub-information depth film because the nitrogen concentration in the bare HA scaffold is higher than in the Kapton covered scaffold (Fig. 4). Considering that the path of the film-forming species from sides and the bottom is at least as long as the path from the top, the higher nitrogen concentration can be explained only by the deposition of additional PPF material and therefore an increase of the PPF thickness.

4.4. Effective sticking probability

The microtrench experiments estimated the effective sticking probability to ≈ 0.1 . Furthermore, the different discharge conditions resulted in a quite similar step coverage. The effective sticking probabilities must then also be similar, although the chemistry of deposited coatings was clearly different. Fig. 6 also shows a large variation of the estimated sticking coefficient η with AR. However, η should not depend on the geometry. This apparent contradiction arises from effects not considered in the derivation of Eq. (1) or in the Monte Carlo simulation, in particular the effect of ion bombardment or species with a different sticking probability.

The effect of ion bombardment can be qualitatively analyzed as follows. Assume that a small fraction of the deposited thickness can be attributed to the ion bombardment, either directly because of mass transport or indirectly due to the formation of bonding sites on the surface. Since the ion bombardment is anisotropic this contribution is the same on the bottom of the trench and outside. The step coverage results should be then corrected by subtracting this contribution from both, the bottom and outside film thicknesses. In the limiting case, the smallest measured SC can be attributed entirely to the effect of ion bombardment. However, the subtraction of this largest possible contribution is still able to correct only the single point with the smallest SC and does not flatten the dependence of effective sticking probability η on AR in the whole range. Therefore, the effect of anisotropic deposition by ion bombardment cannot explain the dependence of η on AR.

In Eq. (1), we assumed only a single film-forming specie, while in reality there is a distribution based on the relative populations and sticking probabilities of all species contributing to the film growth. Since this assumption is not sufficient to cover all experimental results we can construct a second approximation model with two populations of film-forming species with different fractions $1-x$ and x and sticking probabilities η_1 and η_2 . Modifying the Eq. (1) for two populations yields:

$$SC = \frac{1-x}{\cosh\phi_1 + \sqrt{3\eta_1/8}\sinh\phi_1} + \frac{x}{\cosh\phi_2 + \sqrt{3\eta_2/8}\sinh\phi_2}, \quad \phi_i = \frac{H}{W} \sqrt{\frac{3\eta_i}{2}}, \quad i = 1, 2. \quad (3)$$

Similarly, Eq. (2) describing thickness deposited in the macrocavity can be expanded to account for two populations of the film-forming species:

$$\frac{h(y)}{h_0} = (1-x) \frac{\cosh(\alpha_1 y)}{\cosh(\alpha_1 L/2)} + x \frac{\cosh(\alpha_2 y)}{\cosh(\alpha_2 L/2)}, \quad \alpha_i = \frac{1}{H} \sqrt{\frac{3\eta_i}{2}}, \quad i = 1, 2. \quad (4)$$

Since the separate fits of SC and macrocavity data by these models predict similar relative populations and their respective sticking probabilities, we decided to fit all the data together. The result of this global fit is shown in Fig. 6a and 7b as a solid blue line which agrees well with all the experimental data (unlike the single-population model). According to the global fit, 76% of the population has a large sticking probability $\eta_1 = 0.20 \pm 0.01$ and the remaining 24% has a relatively small sticking probability $\eta_2 = 0.0015 \pm 0.0002$. Compared to the simple estimate of η in the range 0.01–0.2, the existence of a significant population of film-forming species with a small sticking probability explains better the relatively large penetration of the deposition into porous materials, albeit depositing only a very thin PPF.

The two-population model also allows us to further discuss the chemistry of film-forming species with different sticking probability. On the macrocavity edge about 75% of the deposited thickness can be attributed to the large sticking probability species, whereas in the center it is only about 4%. The small decrease of [N]/[C] ratio towards the macrocavity center (Fig. 7), therefore, indicates that the species with large η has on average a higher [N]/[C] ratio, but only slightly. Quantifying this estimate gives [N]/[C] ≈ 0.245 and 0.205 for the

populations with η_1 and η_2 , respectively.

The high-resolution C 1s spectra measured in the macrocavity suggest a sharp change in the chemistry at the macrocavity edge. However, as described in Section 3.6, this is probably due to the effect of vertical differential charging in very thin films rather than an effect of the ion bombardment. Since the relative concentrations of the fitted C 1s components are almost constant inside the macrocavity, we conclude that the relative chemistry of functional groups deposited by species with a different sticking probability is quite similar. Furthermore, since the transport mechanism of the film-forming species in the macrocavity is the same as in the porous scaffolds, we can extend these conclusions also to the PPFs deposited into these substrates.

5. Conclusion

We highlighted several aspects that need to be considered when designing a successful plasma polymerization into non-planar geometries, such as culture wells or porous scaffolds and mats. The deposition process was studied for capacitively coupled radio-frequency discharge in the mixture of cyclopropylamine and argon for three different discharge conditions with the varying average RF power. The geometry of the well structures influences both the deposition rate and the chemistry of the CPA plasma polymer films. We showed that the well structures behave differently because of their different aspect ratios. While even relatively wide and shallow wells such as Petri dishes influence the deposition rate, they almost do not alter the film composition. Higher aspect ratio wells, on the other hand, change also the chemistry of the deposited films. In particular, the [N]/[C] ratio is always lower in these wells, although the decrease is relatively small unless the production of powder is observed.

The study of deposition into porous materials showed that the penetration depth is quite large, from tens of micrometers for the PCL mats to hundreds for the HA. The penetration is driven by the Knudsen diffusion of film-forming species enabled by a relatively low effective sticking probability. The observed significant decrease of nitrogen concentration with the thickness of the porous substrates had to be explained by the combination of two effects. First, a similar decrease of [N]/[C] as for the wells has to be expected. Second, the thicknesses of plasma polymer is below the XPS information depth.

The combined analysis of the deposition into microtrenches and a macrocavity lead to the conclusion that the sticking probability of the film-forming species can be sufficiently represented by a two-population model. The model predicts that while the majority of the film-forming species (76%) has a large sticking probability of 0.20 ± 0.01 , still a significant part (24%) has a relatively small sticking probability of 0.0015 ± 0.0002 . The study of average chemistry of the two populations using the diffusion-driven deposition in the macrocavity found only a minor difference. Therefore, we conclude that the deep deposition inside the studied porous substrates is accomplished primarily by the low sticking probability species which yields a plasma polymer with a slightly lower [N]/[C] ratio.

Declaration of Competing Interest

The authors declare that they have no known competing financial interests or personal relationships that could have appeared to influence the work reported in this paper.

Acknowledgement

This research was carried out under the project 18-12774S supported by the Czech Science Foundation, the project CEITEC 2020 (LQ1601) with financial support from the Ministry of Education, Youth and Sports of the Czech Republic under the National Sustainability Programme II. CzechNanoLab project LM2018110 funded by MEYS CR is gratefully acknowledged for the financial support of the measurements and sample

fabrication at CEITEC Nano Research Infrastructure. Authors acknowledge the kind help of Dr. Jiří Vohánka with the ellipsometric mapping.

Appendix A. Supplementary material

Supplementary data associated with this article can be found, in the online version, at <https://doi.org/10.1016/j.apsusc.2020.147979>.

References

- [1] N. Inagaki, Plasma surface modification and plasma polymerization. Plasma surface modification and plasma polymerization, CRC Press, 1996.
- [2] F.F. Shi, Recent advances in polymer thin films prepared by plasma polymerization synthesis, structural characterization, properties and applications, Surf. Coat. Technol. 82 (1) (1996) 1–15.
- [3] K.S. Siow, L. Britcher, S. Kumar, H.J. Griesser, Plasma Methods for the Generation of Chemically Reactive Surfaces for Biomolecule Immobilization and Cell Colonization - A Review, Plasma Processes Polym. 3 (6–7) (2006) 392–418.
- [4] D. Hegemann, Plasma polymerization and its applications in textiles, Indian J. Fibre Text. Res. 1 (2006) 99–115.
- [5] A. Manakhov, M. Landová, J. Medalová, M. Michlíček, J. Polčák, D. Nečas, L. Zajíčková, Cyclopropylamine plasma polymers for increased cell adhesion and growth, Plasma Processes Polym. 14 (7) (2017) 1600123.
- [6] H.K. Yasuda, Some important aspects of plasma polymerization, Plasma Processes Polym. 2 (2005) 293–304.
- [7] D. Hegemann, U. Schütz, A. Fischer, Macroscopic plasma-chemical approach to plasma polymerization of HMDSO and CH₄, Surf. Coat. Technol. 200(1–4) (2005) 458–462.
- [8] D. Hegemann, U. Schütz, E. Körner, Macroscopic approach to plasma polymerization using the concept of energy density, Plasma Processes Polym. 8 (2011) 689–694.
- [9] D. Hegemann, H. Brunner, C. Oehr, Evaluation of deposition conditions to design plasma coatings like SiO_x and a-C:H on polymers, Surf. Coat. Technol. 174–175 (2003) 253–260.
- [10] D. Hegemann, M.M. Hossain, E. Körner, D.J. Balazs, Macroscopic description of plasma polymerization, Plasma Processes Polym. 4 (2007) 229–238.
- [11] D. Hegemann, Macroscopic investigation of reaction rates yielding plasma polymer deposition, J. Phys. D: Appl. Phys. 46 (2013) 205204.
- [12] A. Rutscher, H.E. Wagner, The Model of Macroscopic Kinetics in Non-Equilibrium Plasma Chemical Reactions, Beiträge aus der Plasmaphysik 25 (1985) 315–328.
- [13] C. Corbella, I. Bialuch, M. Kleinschmidt, K. Bewilogua, Up-scaling the production of modified a-C:H coatings in the framework of plasma polymerization processes, Solid State Sci. 11 (10) (2009) 1768–1772.
- [14] T. Desmet, R. Morent, N. De Geyter, C. Leys, E. Schacht, P. Dubruel, Nonthermal plasma technology as a versatile strategy for polymeric biomaterials surface modification: A review, Biomacromolecules 10 (9) (2009) 2351–2378.
- [15] E. Makhneva, A. Manakhov, P. Skládal, L. Zajíčková, Development of effective QCM biosensors by cyclopropylamine plasma polymerization and antibody immobilization using cross-linking reactions, Surf. Coat. Technol. 290 (2016) 116–123.
- [16] D.G. Castner, B.D. Ratner, Biomedical surface science: Foundations to frontiers, Surf. Sci. 500 (1) (2002) 28–60.
- [17] K. Jarvis, S. McArthur, Exploiting reactor geometry to manipulate the properties of plasma polymerized acrylic acid films, Materials 12 (2019) 2597.
- [18] R. Radjef, K. Jarvis, B.L. Fox, S.L. McArthur, Design and characterization of a plasma chamber for improved radial and axial film uniformity, Plasma Processes Polym. (2020) e2000017.
- [19] C. Bergemann, M. Cornelsen, A. Quade, T. Laube, M. Schnabelrauch, H. Rebl, V. Weißmann, H. Seitz, B. Nebe, Continuous cellularization of calcium phosphate hybrid scaffolds induced by plasma polymer activation, Mater. Sci. Eng.: C 59 (2016) 514–523.
- [20] L. Cheng, R. Ghobeira, P. Cools, Z. Liu, K. Yan, N.D. Geyter, R. Morent, Comparative study of different nitrogen-containing plasma modifications applied on 3D porous PCL scaffolds and 2D PCL films, Appl. Surf. Sci. 516 (2020) 146067.
- [21] M.J. Taylor, H. Aitchison, M.J. Hawker, M.N. Mann, E.R. Fisher, D.J. Graham, L. J. Gamble, Time of flight secondary ion mass spectrometry—a method to evaluate plasma-modified three-dimensional scaffold chemistry, Biointerphases 13 (3) (2018) 03B415.
- [22] E.S. Permyakova, P.V. Kiryukhantsev-Korneev, K.Y. Gudzh, A.S. Konopatsky, J. Polcak, I.Y. Zhitnyak, N.A. Gloushankova, D.V. Shtansky, A.M. Manakhov, Comparison of different approaches to surface functionalization of biodegradable polycaprolactone scaffolds, Nanomaterials 9 (12) (2019) 1769.
- [23] X. Liu, Y. Won, P.X. Ma, Surface modification of interconnected porous scaffolds, J. Biomed. Mater. Res. Part A 74A (1) (2005) 84–91.
- [24] N. Yamasaki, M. Hirao, K. Nanno, K. Sugiyasu, N. Tamai, N. Hashimoto, H. Yoshikawa, A. Myoui, A comparative assessment of synthetic ceramic bone substitutes with different composition and microstructure in rabbit femoral condyle model, J. Biomed. Mater. Res. Part B: Appl. Biomater. 91B (2) (2009) 788–798.
- [25] P. Cernochová, L. Blahová, J. Medalová, D. Nečas, M. Michlíček, P. Kaushik, J. Příbyl, J. Bartošková, A. Manakhov, L. Bačáková, L. Zajíčková, Cell type specific adhesion to surfaces functionalised by amine plasma polymers, Scient. Rep. 10 (2020) 9357.

- [26] K.V. Chan, Y. Onyshchenko, M. Asadian, A.Y. Nikiforov, H. Declercq, R. Morent, N. De Geyter, Investigating the stability of cyclopropylamine-based plasma polymers in water, *Appl. Surf. Sci.* 517 (2020) 146167.
- [27] M. Michlíček, A. Manakhov, E. Dvořáková, L. Zajčková, Homogeneity and penetration depth of atmospheric pressure plasma polymerization onto electrospun nanofibrous mats, *Appl. Surf. Sci.* 471 (2019) 835–841.
- [28] D. Franta, D. Nečas, L. Zajčková, Models of dielectric response in disordered solids, *Opt. Exp.* 15 (24) (2007) 16230–16244.
- [29] D. Nečas, I. Ohlídal, D. Franta, Variable-angle spectroscopic ellipsometry of considerably non-uniform thin films, *J. Opt.* 13 (8) (2011) 085705.
- [30] F. Truica-Marasescu, M.R. Wertheimer, Nitrogen-rich plasma-polymer films for biomedical applications, *Plasma Processes Polym.* 5 (1) (2008) 44–57.
- [31] H. Komiyama, Y. Shimogaki, Y. Egashira, Chemical reaction engineering in the design of CVD reactors, *Chem. Eng. Sci.* 54 (13) (1999) 1941–1957.
- [32] G. Beamson, A. Bunn, D. Briggs, High-resolution monochromated XPS of poly (methyl methacrylate) thin films on a conducting substrate, *Surf. Interface Anal.* 17 (2) (1991) 105–115.
- [33] D. Hegemann, M. Michlíček, N.E. Blanchard, U. Schütz, D. Lohmann, M. Vandenbossche, L. Zajčková, M. Drábik, Deposition of functional plasma polymers influenced by reactor geometry in capacitively coupled discharges, *Plasma Processes Polym.* 13 (2) (2016) 279–286.
- [34] D. Hegemann, E. Körner, S. Guimond, Plasma polymerization of acrylic acid revisited, *Plasma Processes Polym.* 6 (4) (2009) 246–254.
- [35] N.E. Blanchard, B. Hanselmann, J. Drosten, M. Heuberger, D. Hegemann, Densification and Hydration of HMDSO Plasma Polymers, *Plasma Processes Polym.* 12 (1) (2015) 32–41.
- [36] M. Santos, B. Reeves, P. Michael, R. Tan, S.G. Wise, M.M.M. Bilek, Substrate geometry modulates self-assembly and collection of plasma polymerized nanoparticles, *Commun. Phys.* 52 (2) (2019).
- [37] Ž. Gosar, J. Kovač, D. Donlagić, S. Pevec, G. Primc, I. Junkar, A. Vesel, R. Zaplotnik, PECVD of hexamethyldisiloxane coatings using extremely asymmetric capacitive RF discharge, *Materials (Basel)* 13 (9) (2020).
- [38] V.N. Burganos, S.V. Sotirchos, Simulation of Knudsen diffusion in random networks of parallel pores, *Chem. Eng. Sci.* 43 (7) (1988) 1685–1694.